

# Design, Theoretical, and Experimental Investigation of Tensile-Strained Germanium Quantum-Well Laser Structure

Mantu K. Hudait,\* Felipe Murphy-Armando, Dzianis Saladukha, Michael B. Clavel, Patrick S. Goley, Deepam Maurya, Shuvodip Bhattacharya, and Tomasz J. Ochalski



Cite This: *ACS Appl. Electron. Mater.* 2021, 3, 4535–4547



Read Online

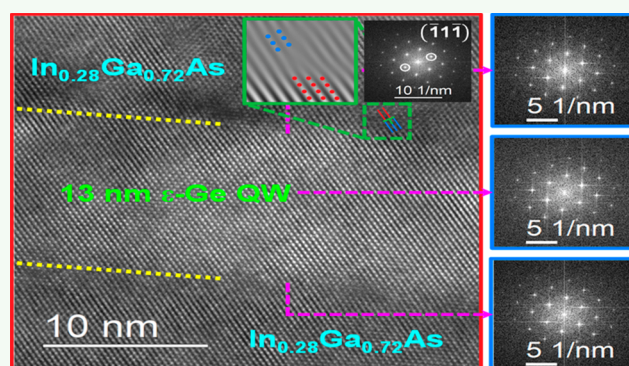
ACCESS |

Metrics & More

Article Recommendations

**ABSTRACT:** Strain and band gap engineered epitaxial germanium ( $\epsilon$ -Ge) quantum-well (QW) laser structures were investigated on GaAs substrates theoretically and experimentally for the first time. In this design, we exploit the ability of an InGaAs layer to simultaneously provide tensile strain in Ge (0.7–1.96%) and sufficient optical and carrier confinement. The direct band-to-band gain, threshold current density ( $J_{th}$ ), and loss mechanisms that dominate in the  $\epsilon$ -Ge QW laser structure were calculated using first-principles-based 30-band k-p electronic structure theory, at injected carrier concentrations from  $3 \times 10^{18}$  to  $9 \times 10^{19} \text{ cm}^{-3}$ . The higher strain in the  $\epsilon$ -Ge QW increases the gain at higher wavelengths; however, a decreasing thickness is required by higher strain due to critical layer thickness for avoiding strain relaxation. In addition, we predict that a  $J_{th}$  of  $300 \text{ A/cm}^2$  can be reduced to  $<10 \text{ A/cm}^2$  by increasing strain from 0.2% to 1.96% in  $\epsilon$ -Ge lasing media. The measured room-temperature photoluminescence spectroscopy demonstrated direct band gap optical emission, from the conduction band at the  $\Gamma$ -valley to heavy-hole (0.6609 eV) from 1.6% tensile-strained Ge/ $\text{In}_{0.24}\text{Ga}_{0.76}\text{As}$  heterostructure grown by molecular beam epitaxy, is in agreement with the value calculated using 30-band k-p theory. The detailed plan-view transmission electron microscopic (TEM) analysis of 0.7% and 1.2% tensile-strained  $\epsilon$ -Ge/ $\text{InGaAs}$  structures exhibited well-controlled dislocations within each  $\epsilon$ -Ge layer. The measured dislocation density is below  $4 \times 10^6 \text{ cm}^{-2}$  for the 1.2%  $\epsilon$ -Ge layer, which is an upper bound, suggesting the superior  $\epsilon$ -Ge material quality. Structural analysis of the experimentally realistic 1.95% biaxially strained  $\text{In}_{0.28}\text{Ga}_{0.72}\text{As}/13 \text{ nm } \epsilon\text{-Ge}/\text{In}_{0.28}\text{Ga}_{0.72}\text{As}$  QW structure demonstrated a strained Ge/ $\text{In}_{0.28}\text{Ga}_{0.72}\text{As}$  heterointerface with minimal relaxation using X-ray and cross-sectional TEM analysis. Therefore, our monolithic integration of a strained Ge QW laser structure on GaAs and ultimately the transfer of the process to the Si substrate via an  $\text{InGa(Al)As/III-V}$  buffer architecture would provide a significant step toward photonic technology based on strained Ge on a Si platform.

**KEYWORDS:** germanium, epitaxy, molecular beam epitaxy, heterostructure, laser



## INTRODUCTION

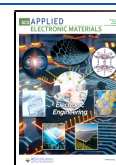
The integration of group-IV-based (e.g., Ge, SiGe, GeSn) light sources on a silicon (Si) substrate has been intensively studied for decades without technological impact. It was believed that this lack of success was due to the quality of material synthesis and approaches taken to demonstrate the light sources on Si. However, excellent progress has been made in recent years for the development of group-IV-based light sources,<sup>1–13</sup> opening up the possibility to have a major impact in the optoelectronic research field. In particular, the development of novel short-wavelength near-infrared (NIR) tunable laser sources, in the range 1.7–2.5  $\mu\text{m}$ , is important for optical coherence tomography (OCT) and biomedical applications.<sup>14–17</sup> It has recently been discovered with noncoherent light that the spectrum in the short-wavelength infrared (SWIR) can achieve

a much higher resolution and penetration in opaque living tissue than NIR, especially in brain tissue imaging.<sup>14–17</sup> In OCT, another property affecting the resolution is the emission bandwidth: the wider the bandwidth, the higher the resolution achievable. However, there are a lack of sources in the SWIR that have the combination of desired intensity and bandwidth to further enhance OCT in this spectral range. In addition, in the current Si microprocessors, copper interconnect bottle-

Received: July 25, 2021

Accepted: September 27, 2021

Published: October 14, 2021



necks due to resistive power loss for both interchip and intrachip communication are calling for integrated light sources. A desirable alternative would be on-chip integrated photonic devices with Si CMOS technology. However, indirect band gap semiconductors, Si and Ge, are usually unsuitable for laser diodes due to their inefficient radiative recombination. In the work reported in ref 18, a single 1183 nm continuous-wave *off-chip* solid-state laser acts as the light source for the demonstration of an electronic–photonic microprocessor chip that enables VLSI technology, by adding nanophotonics as a new design dimension. It has also been proposed that photonic devices to be integrated directly with electronics in the CMOS process enabled a fully functioning electronic–photonic system on a single chip to be produced in a high-volume electronics foundry. To achieve such an aggressive goal, extensive research was pursued on GeSn materials as a function of tin (Sn) alloy composition<sup>1–13,19–31</sup> on Si or GeSn bonded with a virtual substrate as well as III–V lasers grown on<sup>26,32,33</sup> or bonded to a Si<sup>19</sup> substrate. Liu et al.<sup>34</sup> played the thermal mismatch between the deposited Ge layer and the Si substrate that results in a  $\sim 0.2\%$  tensile strain in the Ge layer during material synthesis combined with *n*-type doping ( $\geq 7 \times 10^{19} \text{ cm}^{-3}$ ) in order to compensate the pseudo-energy-difference between the  $\Gamma$ - and L-valley ( $\sim 120 \text{ meV}$ ) at the conduction band for the emission wavelength of  $1.55 \mu\text{m}$ . This approach resulted in a weak optical gain and emission from the direct gap transition of a deposited Ge layer. Although this research work is promising, the defects and dislocations due to lattice mismatch in the active Ge lasing media on Si in addition to the fixed laser wavelength due to the fixed strain/doping suggest that an alternative approach for a tunable wavelength Ge laser on Si is needed. The modification could be the Ge-based quantum-well (QW) configuration with proper barrier layers such that they will provide both carrier confinement (through valence and conduction band offsets) and optical confinement (through differences in refractive indices) and hence achieve low threshold current density ( $J_{\text{th}}$ ) and high efficiency ( $\eta$ ). This hybrid integration of a strained Ge ( $\epsilon$ -Ge) QW design through barrier materials-based electronic–ptoelectronic devices with Si CMOS technology would revolutionize technology needs in the near future.

In this paper, we have designed and demonstrated a 1.95% strained Ge QW laser structure ( $\text{In}_{0.28}\text{Ga}_{0.72}\text{As}/13 \text{ nm } \epsilon\text{-Ge}/\text{In}_{0.28}\text{Ga}_{0.72}\text{As}$ ) through modeling and experimentally via strain and a band-gap-engineered epitaxial Ge layer using an interconnected dual chamber solid source molecular beam epitaxy (MBE) deposition system. This method offers design flexibility to provide tunable strain to Ge and hence the band gap, by changing indium (In) composition in the  $\text{In}_x\text{Ga}_{1-x}\text{As}$  barrier materials during material synthesis. In addition, this approach provided direct band gap Ge and type-I band alignment,<sup>35</sup> both being needed for carrier and optical confinement. These Ge QW laser structures were characterized using high-resolution X-ray diffraction for strain analysis and structural properties, and cross-sectional and plan-view transmission electron microscopy (TEM) for defect properties. The room-temperature optical properties using photoluminescence (PL) spectroscopy, materials analysis, and Ge laser modeling using FIMMWAVE<sup>36</sup> were demonstrated as a first step toward the development of Ge-based light sources. Therefore, our monolithic heterogeneous integration of a tunable wavelength Ge laser structure (via strain and band gap engineering) on GaAs and ultimately the transfer of the process to a Si

substrate using an  $\text{InGa}(\text{Al})\text{As}/\text{III-V}$  buffer architecture<sup>31,37–41</sup> would provide a paradigm shift for photonic technology on Si.

## RESULTS AND DISCUSSION

**Strain Dependent  $\epsilon$ -Ge/ $\text{In}_x\text{Ga}_{1-x}\text{As}$  Electronic Structure Calculations.** The first step in demonstrating that strained  $\epsilon$ -Ge can produce an enhancement in optical gain is determining the strain and layer thickness conditions that increase direct band electron–hole recombination. Figure 1

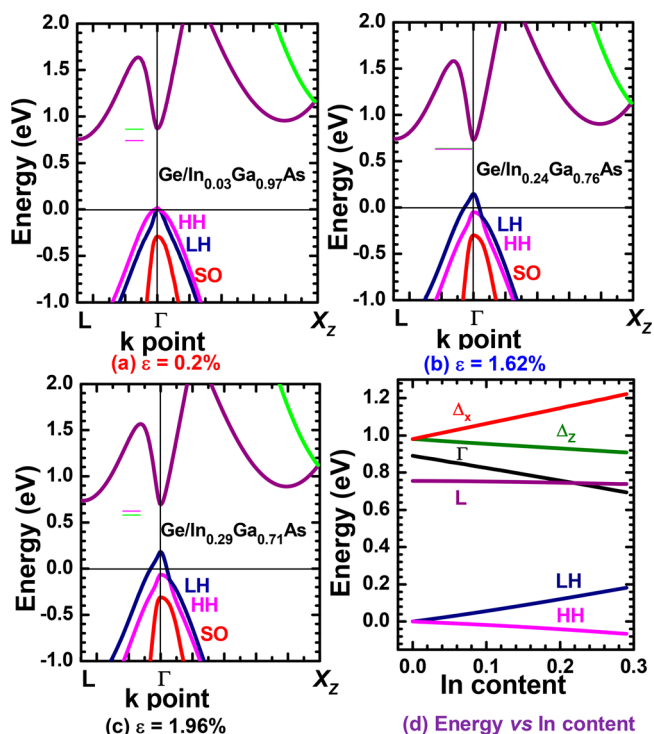


**Figure 1.** Electronic band structure of strained Ge calculated using a 30-band *k*-*p* approach at 0 K. Biaxial strain applied is (a) 0.2%, (b) 1.62%, and (c) 1.96%.  $X_z$  is the X point in the direction of growth. The inset shows the energy difference of the conduction band minimum on the left (L) and the gamma point ( $\Gamma$ ) in each strain amount. At 1.96% strain level, the  $\Gamma$  point is lower than the L point in the conduction band. (d) Theoretical band gap versus indium (In) dependence of the  $\text{Ge}/\text{In}_x\text{Ga}_{1-x}\text{As}$  system, and the indirect to direct band gap of Ge occurs at about 22–24% In composition in  $\text{In}_x\text{Ga}_{1-x}\text{As}$ .

shows the calculated electronic band structure of Ge with applied (100) biaxial strain corresponding to Ge grown on  $\text{In}_x\text{Ga}_{1-x}\text{As}$  at different In concentrations, which correspond to those grown and studied in this work. In terms of band structure, optical gain depends on the competition between the single  $\Gamma$  and the four L conduction band valleys in Ge. In unstrained bulk Ge, the minimum of the conduction band is at the four L-valleys, while the direct  $\Gamma$ -valley lies 120 meV above the L-valley minimum (see Figure 1a). Biaxial tensile strain lowers the  $\Gamma$ -valley, reaching the indirect-to-direct conduction band transition at In content  $x = 0.24$ , corresponding to a strain of  $\epsilon = 1.62\%$ , and is consistent with previous observations.<sup>31,40</sup> Further strain turns Ge into a direct band semiconductor. The separation between the L-valley and  $\Gamma$ -valley with increasing strain, as indicated by green and pink lines (by increasing indium content in the  $\text{In}_x\text{Ga}_{1-x}\text{As}$  layer) in

each case, is shown in the inset of Figure 1. It is important to note that the density of states (DOS) of the L-valley is  $\sim 50$  times larger than that of the  $\Gamma$ -valley, including the 4-fold degeneracy (see the much larger effective mass of the L-valley relative to the  $\Gamma$ -valley in the energy dispersion shown in Figure 1a). Therefore, most of the injected electrons will populate the L-valley unless strain can induce enough separation between the valleys. Lowering the  $\Gamma$ -valley sufficiently below the L-valley (see Figure 1c) so that most injected electrons populate the  $\Gamma$ -valley should see a very large increase in gain. However, gain will increase at longer wavelengths and lower injection densities than in bulk Ge with any lowering of the conduction band  $\Gamma$ -valley, as this is the only direct-band recombination channel. The high strains required to sufficiently lower the  $\Gamma$ -valley to capture most injected carriers may limit the thickness of the  $\epsilon$ -Ge that can be grown, due to critical thickness constraints. As we will see later, quantum confinement pushed the  $\Gamma$ -valley (see Figure 1d) higher in energy faster than the L-valley, due to the small effective mass of the  $\Gamma$ -valley. Therefore, the thickness at which the Ge active layer can be grown will play a crucial role in the gain achievable in a group-IV-based QW laser.

### $\epsilon$ -Ge Quantum-Well Laser Design and Modeling: Selection of Thickness, Strain, and Doping Density.

Figure 2 shows the band gap and 1.95% tensile-strain-

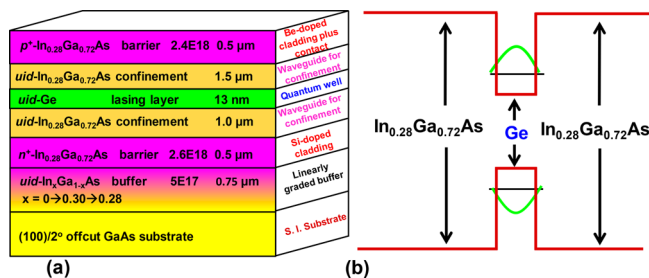


**Figure 2.** (a) Ge laser structure on GaAs with a tunable surface lattice constant of a mixed-cation InGaAs ternary buffer layer architecture. The III–V optical cavity is also designed for the tunable wavelength Ge laser structure. (b) Schematic representation of the energy band diagram for the In<sub>0.28</sub>Ga<sub>0.72</sub>As/ $\epsilon$ -Ge/In<sub>0.28</sub>Ga<sub>0.72</sub>As laser structure (it is not to scale).

engineered Ge QW laser structure on a GaAs substrate as well as a schematic representative energy band diagram using an In<sub>x</sub>Ga<sub>1-x</sub>As strain template along with an In<sub>0.28</sub>Ga<sub>0.72</sub>As carrier and optical confinement layer. This Ge QW laser structure was modeled using the FIMMWAVE mode solver from Photon Design.<sup>36</sup> This FIMMWAVE provides a full vectorial mode solver suitable for modeling the waveguide and the grating structures with different geometries. In the Ge laser structure, the In composition in linearly graded In<sub>x</sub>Ga<sub>1-x</sub>As buffer can be varied to a targeted In composition for achieving a different tensile-strained amount in Ge. This in turn changes the strain-induced band gap of Ge and hence the lasing wavelength. One can replace the InGaAs cladding/waveguide layer by the InAlAs/AlGaInAs layer in the Ge QW laser structure for superior optical and carrier confinement due to its larger band offsets and differences in refractive indexes. In our design, we exploit the ability of Ge/III–V heterostructures to induce epitaxial stress in the Ge thin film and simultaneously provide sufficient optical and carrier confinement so as to realize a practical lasing structure. A first-principles computa-

tion of the Ge/InAlAs electronic structure reveals band offsets  $\geq 0.56 \pm 0.1$  eV at the  $\epsilon$ -Ge/In<sub>x</sub>Al<sub>1-x</sub>As heterointerface,<sup>42</sup> corroborated with our experimental band offset results. Utilizing an MBE growth process, discussed below, we have demonstrated the feasibility of integrating the tensile-strained In<sub>x</sub>Ga<sub>1-x</sub>As/ $\epsilon$ -Ge/In<sub>x</sub>Ga<sub>1-x</sub>As QW laser structure on a GaAs substrate. The 13 nm  $\epsilon$ -Ge layer was embedded within lower refractive index layers of InGaAs for confining the optical mode and maximizing mode intensity at the intrinsic region of the heterostructure. In the center of the optical waveguide, the  $\epsilon$ -Ge QW will provide a confinement for electrons and holes. One of the most critical design parameters for the Ge laser structure is the optical cavity and the active material. The specific thickness of the optical waveguide and finally the laser source geometry can be designed and optimized by employing the eigenmode solution methods build in FIMMWAVE.<sup>36</sup>

Figure 3 shows the simulated energy density profiles and transverse electric (TE) mode of a 1.95% strained  $\epsilon$ -Ge QW structure. The laser mode is confined in the InGaAs layers above and below the active  $\epsilon$ -Ge lasing medium, shown in Figure 3a,b. Vertical and horizontal energy density profiles visualize the intensity drop to the edges of the InGaAs layers. According to vertical cross-section in the center of mode,  $\sim 84\%$  of TE mode is confined in the undoped In<sub>0.28</sub>Ga<sub>0.72</sub>As region. In addition, the mode penetration is higher into the bottom InGaAs layer, and it was due to the abrupt refractive index change from the top InGaAs layer to air at the upper as compared to the bottom barrier layer. However, the majority of the TE mode can be confined within the  $\epsilon$ -Ge layer (it depends on the layer thickness and amount of strain) by inserting a large band gap Al<sub>0.3</sub>In<sub>0.28</sub>Ga<sub>0.42</sub>As (lower refractive index) layer on both sides of the In<sub>0.28</sub>Ga<sub>0.72</sub>As/ $\epsilon$ -Ge/In<sub>0.28</sub>Ga<sub>0.72</sub>As lasing media, as shown in Figure 4. The refractive index of each layer is also included for a better understanding of the optical confinement. In this structure, the total In<sub>0.28</sub>Ga<sub>0.72</sub>As layer thickness in each side of  $\epsilon$ -Ge is divided into a combination of In<sub>0.28</sub>Ga<sub>0.72</sub>As and Al<sub>0.3</sub>In<sub>0.28</sub>Ga<sub>0.42</sub>As layers. Here, the Al<sub>0.3</sub>In<sub>0.28</sub>Ga<sub>0.42</sub>As layer acts as a separate confinement heterostructure (SCH), and the large differences in refractive indices between the  $\epsilon$ -Ge and the Al<sub>0.3</sub>In<sub>0.28</sub>Ga<sub>0.42</sub>As barrier layer prevent the optical mode penetration onto the bottom and upper InGaAs layer, supported by the simulated optical mode, shown in Figure 5. The ternary InGaAs layer on both sides of the  $\epsilon$ -Ge layer is for the ease of the growth of the Ge QW laser structure during the MBE growth process as compared to the direct growth of a quaternary Al<sub>0.3</sub>In<sub>0.28</sub>Ga<sub>0.42</sub>As layer on the top of the  $\epsilon$ -Ge layer. The bottom Al<sub>0.3</sub>In<sub>0.28</sub>Ga<sub>0.42</sub>As layer growth is trivial as compared to the upper Al<sub>0.3</sub>In<sub>0.28</sub>Ga<sub>0.42</sub>As layer due to the competition of the adatom mobility of each constituent on the surface at the growth temperature. Note that aluminum (Al) adatom mobility on the growth surface is lower than either In or Ga<sup>43</sup> and thus needs a higher growth temperature than the In or Ga containing film. Therefore, the combination of the Al<sub>0.3</sub>In<sub>0.28</sub>Ga<sub>0.42</sub>As/In<sub>0.28</sub>Ga<sub>0.72</sub>As barrier layer on the  $\epsilon$ -Ge laser structure is indispensable for the consideration of growth as well as both carrier and optical confinement.

Laser efficiency is in large part determined by the dynamics of the carriers in the Ge lasing layer. Using a first-principles 30-band  $k$ - $p$  electronic structure theory approach,<sup>25,40,44</sup> we have determined the optical gain, threshold current density  $J_{th}$ , and loss mechanisms that dominate the laser structure. The direct band-to-band gain ( $G$ ) was calculated using the full band

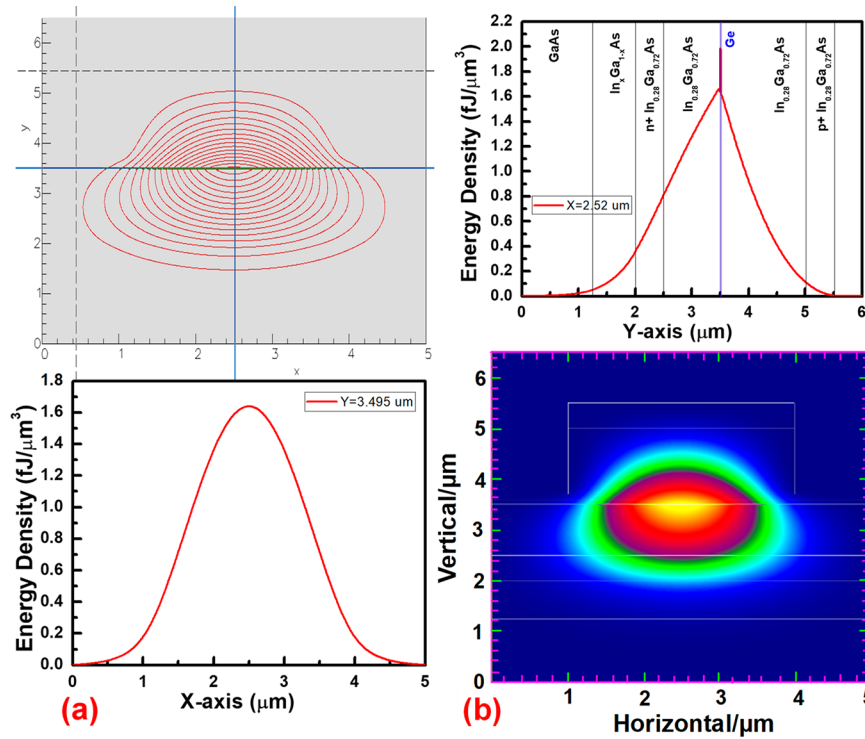


Figure 3. Simulated (a) energy density profiles and (b) TE mode of the 1.95% ε-Ge laser structure using FIMMWARE.

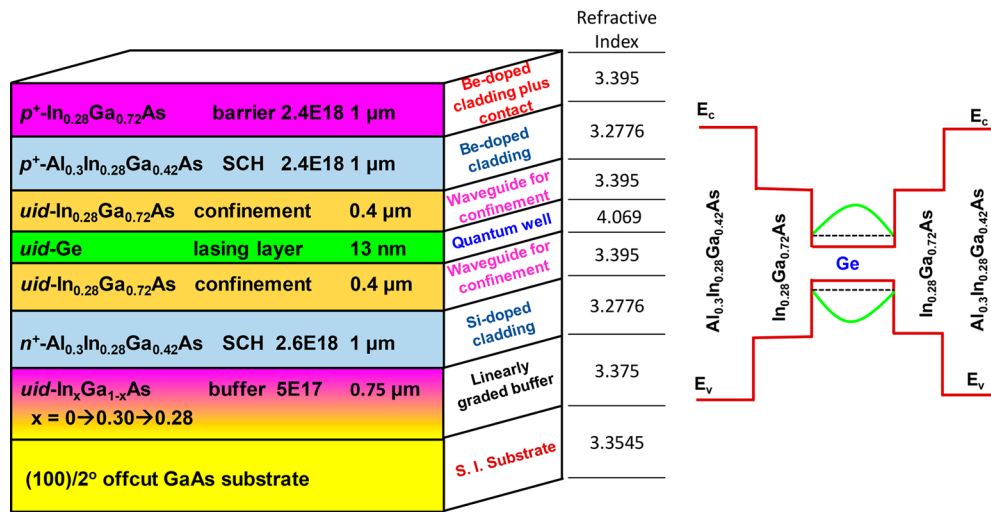


Figure 4. 1.95% strained Ge laser structure on a GaAs substrate with InGaAs ternary buffer. The AlInGaAs layer on both sides of ε-Ge lasing media is for superior optical and carrier confinement, which is acting as a separate confinement heterostructure. The large difference in refractive index between Ge lasing media and the adjacent AlInGaAs barrier layer is to provide an optical confinement. The schematic energy band diagram for the ε-Ge laser structure is shown on the right (it is not to scale).

structure of Ge at three strain configurations (0.2%, 1.62%, and 1.96%) including quantum confinement which are shown in Figure 6 at different injected carrier concentrations in the range from  $3 \times 10^{18}$  to  $9 \times 10^{19} \text{ cm}^{-3}$ . The gain,  $G$ , is calculated using<sup>1</sup>

$$G = \frac{\nu}{\epsilon_0 n_b c \hbar V \gamma} \sum_{k,n,n'} |P_{k,n,n'}|^2 (f_{k,n}^c - f_{k,n'}^v - 1) \text{sech}(\omega_{k,n,n'} - \nu) \quad (1)$$

where  $\nu$  is the laser frequency,  $V$  is the active region volume,  $n_b$  is the background refractive index,  $\gamma$  is the dephasing rate (see ref 1),  $\epsilon_0$  and  $c$  are the permittivity and the speed of light in a vacuum, and  $|P_{k,n,n'}|^2$  is the dipole matrix for optical transition between crystal momentum  $k$ -points in the  $n$  conduction  $\Gamma$ -

valley and  $n'$  heavy hole (HH)/light hole (LH) valleys. Finally, the contribution to the current density ( $J_{sp}$ ) from spontaneous emission was calculated using<sup>1</sup>

$$J_{sp} = ed \int_0^\infty d\nu \left( \frac{n_b \nu}{\pi c} \right)^2 G(\nu) \left[ \exp\left( \frac{\hbar \nu - \mu_{eh}}{k_B T} \right) - 1 \right]^{-1} \quad (2)$$

where  $d$  is the active region thickness,  $\mu_{eh}$  is the electron–hole quasichemical potential energy separation that satisfies the transparency condition in the gain spectrum  $G(\nu) = 0$  at a given carrier concentration, and  $k_B$  is the Boltzmann constant. To our knowledge, these are the first results that consider the

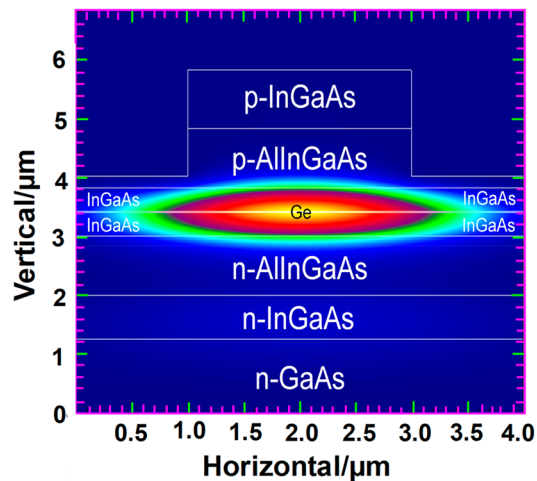


Figure 5. Simulated optical mode in the 1.92%  $\epsilon$ -Ge QW laser structure, shown in Figure 4, using FIMMWAVE.

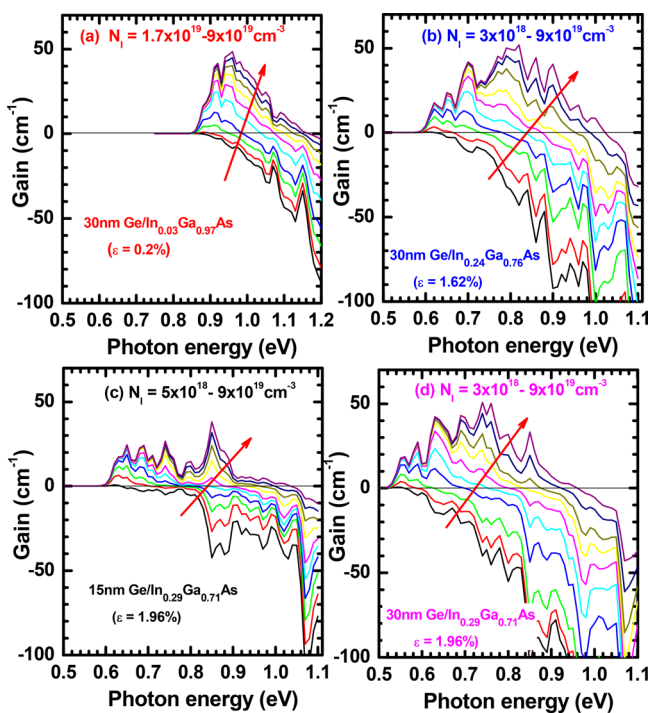


Figure 6. Calculated optical gain vs photon energy at 300 K at various injected carrier densities  $N_i$  for (a) 30 nm Ge/In<sub>0.03</sub>Ga<sub>0.97</sub>As, with  $\epsilon = 0.2\%$  strain; (b) 30 nm Ge/In<sub>0.24</sub>Ga<sub>0.76</sub>As, with  $\epsilon = 1.62\%$  strain; (c) 15 nm Ge/In<sub>0.29</sub>Ga<sub>0.71</sub>As, with  $\epsilon = 1.96\%$  strain; and (d) 30 nm Ge/In<sub>0.29</sub>Ga<sub>0.71</sub>As, with  $\epsilon = 1.96\%$  strain. The injected carrier density,  $N_i$ , for each strain level is indicated in each panel. Here, higher strain increases the gain at higher wavelengths and lower injection concentrations, and  $>1.6\%$  strained with at least 30 nm Ge are needed for achieving higher gain at a lower injection level.

entire electronic band structure for the calculation of gain in this material. We observe that higher strain increases the gain at higher wavelengths and lower injection concentrations. Note that the lowest injected carrier density is different for each figure due to the gain starting at different injections for the different strain-induced band structures. The injected carrier density ( $N_i$ ) for each strain level is indicated in Figure 6. In addition, the decreasing Ge thickness, required by higher strain due to critical layer thickness to avoid strain relaxation, can

remove some of the advantages (i.e., gain) achieved by the strain. In order to address this, we have calculated the gain for 1.96% strained Ge at thicknesses of 15 and 30 nm, respectively, shown in Figure 6c,d. We found that the 1.62% or 1.96% strained Ge with 30 nm Ge layer thickness is among the best for gain as a function of photon energy, with gain also starting at lower injection carrier density. A Ge layer thickness of at least 30 nm and a strain level of  $>1.6\%$  are needed for achieving higher gain at lower  $N_i$ . The trade-off is between the achievable strained Ge thickness with highest tensile strain inside the Ge during growth, and the Ge layer thickness that must be reduced with higher strain to prevent strain relaxation in the tensile-strained Ge QW laser structure. Figure 7 shows

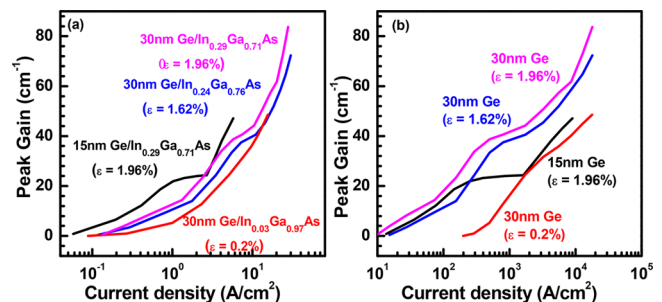
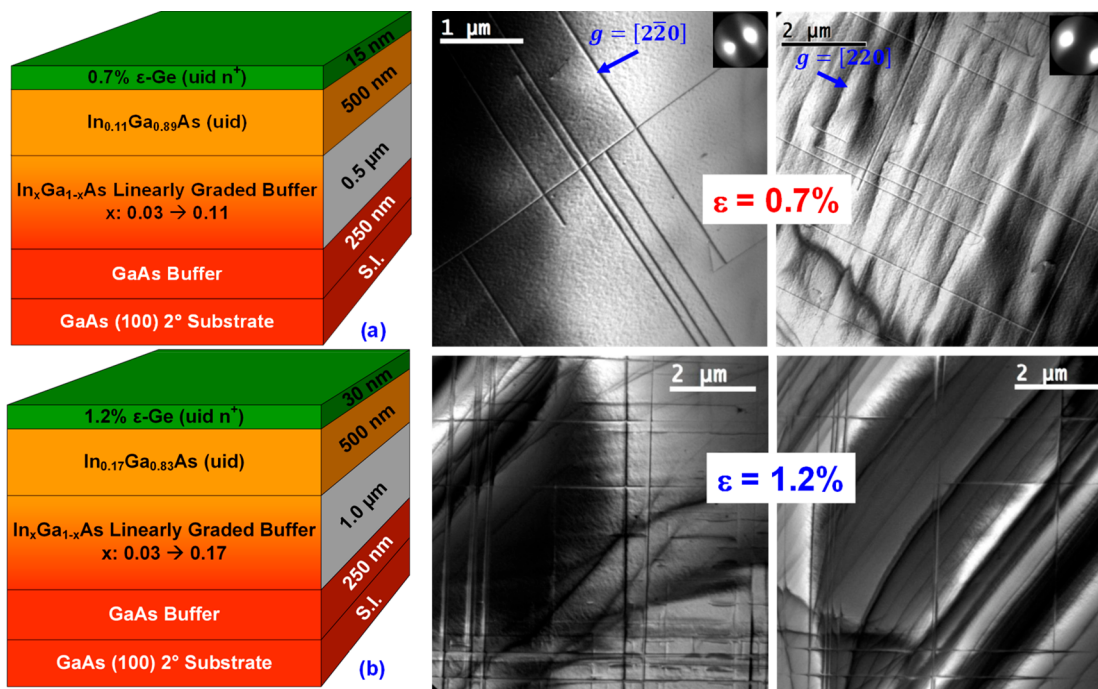


Figure 7. Calculated peak gain vs current density for three strain configurations. The current density is calculated (a) without and (b) with losses arising from nonradiative recombination.

the calculated maximum  $G$  obtained in the simulations shown in Figure 6 versus the current density ( $J_{sp}$ ): (a) where losses in the current are ignored and (b) which includes an estimate of the losses due to Shockley–Read–Hall and Auger recombination processes based on data from ref 1. To date, no reliable models of the free carrier absorption exist for this strained Ge material. We find that increasing strain from 0.2% to 1.62% can dramatically reduce  $J_{th}$  from 300 to  $<10$  A/cm<sup>2</sup>, respectively. If we disregard losses, increasing the strain further to 1.96% reduces the threshold current density even further, shown in Figure 7b. This gain in effectiveness is reduced to that of 1.62% if we include losses. This reduction in effectiveness is a direct consequence of the limit to the Ge QW thickness with higher strain inside the Ge layer. The thinner QW results in a smaller density of states and quantization effect, which limits the gain (see the difference in effective masses due to curvature change by strain in Figure 1). On the other hand, if a 1.96% strain is achieved at thicknesses  $\geq 20$  nm, the gain/threshold current ratio would be much superior as compared to the same thickness and less strain, thanks to the higher direct band gap nature of Ge at higher strain. Therefore, one can find from the first-principles calculation that the gain increases with lower energy for 1.96% strained Ge with increasing Ge thickness from 15 to 30 nm, and the threshold current density decreases with increasing strain and thickness, studied here. Thus, one needs to account for a feedback from experiments to realize a realistic model of the emission in this laser material.

**Materials Analysis of  $\epsilon$ -Ge and  $\epsilon$ -Ge Laser Structure.** *Defect Analysis of  $\epsilon$ -Ge Epilayers via Plan-View TEM.* As we have showcased in Figure 7, there is need for direct band gap Ge for light sources via strain engineering; we have experimentally demonstrated the tunable tensile-strained epitaxial  $\epsilon$ -Ge layers in the strain ranges from 0.0% to 1.95%<sup>31,35,38–40</sup> on GaAs and Si substrates using an InGaAs



**Figure 8.** PV-TEM micrographs of (a) 0.7%  $\epsilon$ -Ge and (b) 1.2%  $\epsilon$ -Ge along with their material growth structure, respectively. The misfit dislocation (MD) networks due to strain relaxation of buffer for each strain amount are clearly visible, implying superior growth of the metamorphic buffer layer and tensile-strained Ge on top of each strain amount.

strain template as well as 1.6% and 1.95% strained InGaAs/ $\epsilon$ -Ge/InGaAs QW structures on linearly graded  $\text{In}_x\text{Ga}_{1-x}\text{As}$  metamorphic buffer using solid source MBE. These structures were characterized using different analytical tools<sup>31,35,38–40</sup> to access the material quality. In this aspect, the defect analysis using plan-view transmission electron microscopy (PV-TEM) is indispensable since the defects can cause the losses in the  $\epsilon$ -Ge lasing media, as shown in Figure 7b. Thus, the determination of the defect density is of utmost importance for mismatch epitaxy especially the tensile-strained Ge layer. Figure 8a,b shows the 0.7%  $\epsilon$ -Ge and 1.2%  $\epsilon$ -Ge layer structures grown on GaAs substrates using a graded  $\text{In}_x\text{Ga}_{1-x}\text{As}$  strain template and PV-TEM micrographs of each structure. It is worth noting that the MBE grown  $\epsilon$ -Ge epilayer thicknesses, 15 nm ( $\epsilon$ -Ge/ $\text{In}_{0.11}\text{Ga}_{0.89}\text{As}$ ) and 30 nm ( $\epsilon$ -Ge/ $\text{In}_{0.17}\text{Ga}_{0.83}\text{As}$ ), remain well below the calculated critical layer thickness values, as we have recently reported<sup>35</sup> using People and Bean's energy balance model.<sup>45</sup> Therefore, it is expected that the strain relaxation in the epitaxial  $\epsilon$ -Ge would be minimal which can cause additional defects and dislocations. The dark band in each figure is the bend contour, which is due to the lattice moving into and out of different Bragg diffraction conditions. The two-dimensional misfit dislocation (MD) networks were clearly visible from each structure and are running in the two  $\langle 110 \rangle$  orthogonal direction. Depending on their Burger vector orientation of these MDs (i.e., parallel, antiparallel, perpendicular, etc.), different types of interactions were possible.<sup>46</sup> In one such interaction, where Burger vectors are perpendicular, no L-reaction (i.e., no  $\alpha$  and  $\beta$  dislocations cross-slip) is anticipated. One can find from Figure 8a,b the different misfit dislocation densities and the character of the dislocation network. Upon inspecting this figure, we found that the 1.2%  $\epsilon$ -Ge sample showed an array of dislocations similar to 0.7%  $\epsilon$ -Ge but with much longer dislocation segments that were closely spaced. As

we know, the local strain fields of MDs are expected to occasionally react when orthogonal MDs intersect. These strain field reactions can cause MDs to repel each other resulting in L-reactions (both MDs change their glide direction by  $90^\circ$ ).<sup>47</sup> L-reactions are statistically expected to occur at 16–25% of MD intersections in diamond and zincblende materials when all dislocations have the usual  $\mathbf{b} = 1/2 \langle 110 \rangle$  type Burgers vectors. Here, we counted no L-reactions for both the 1.2%  $\epsilon$ -Ge and 0.7%  $\epsilon$ -Ge tensile-strained Ge/InGaAs material system. We will explain the absence of L-reactions in this tensile system. The MDs in diamond or zincblende materials glide in  $\{111\}$  slip planes and have Burgers vectors of the type  $\mathbf{b} = 1/2 \langle 110 \rangle$  usually angled  $60^\circ$  from the dislocation line. Normally, such dislocations can easily cross-slip from one  $\{111\}$  plane to another. However, these MDs can also disassociate into Shockley partial dislocation (SPD) pairs with Burgers vectors of the type  $\mathbf{b} = 1/6 \langle 112 \rangle$ . Furthermore, although it has not yet been shown in the Ge/InGaAs material system, MD disassociation has been shown to occur in tensile (100) oriented films in other material systems.<sup>48–52</sup> This is due to the fact that, in the (100) tensile system, the leading Shockley partial dislocation of an SPD pair, the  $90^\circ$  partial is a pure edge component and has its Burgers vector completely aligned with the resolved shear stress on the  $\{111\}$  planes; i.e., the misfit stress acts on the  $90^\circ$  partial very efficiently. Other configurations where this occurs are compressive (110) and (111) growth.<sup>49</sup> Due to the alignment of the leading SPD Burgers vector and the resolved shear stress, MDs nucleate more easily in these configurations, resulting in a downward shift in the critical layer thickness compared to compressive (100) growth.<sup>52,53</sup> If the MDs near the surface were disassociated, it would help explain their straightness since an SPD is unlikely to exhibit cross-slip. We will explain the contrast of two orthogonal MDs below. Therefore, the absence of L-reactions in the dislocation networks in the 1.2%  $\epsilon$ -Ge and

0.7%  $\epsilon$ -Ge system is attributed to these networks being primarily disassociated  $60^\circ$  dislocations. This also implies the superior growth of relaxed metamorphic graded InGaAs buffer layer in each case and subsequently the tensile-strained Ge layer growth on top of each graded buffer. This PV-TEM micrographs also allows us to determine the defect density of  $\sim 1.2 \times 10^7$  and  $< 4 \times 10^6 \text{ cm}^{-2}$  for 0.7% and 1.2% strain, respectively. These TDD values are likely an upper bound, since it can also include TDDs from within the InGaAs virtual substrate, which complicates the accurate assignment of the dislocation density number solely within the  $\epsilon$ -Ge layer. However, we have performed the defect analysis by the invisibility criterion  $\mathbf{g} \cdot \mathbf{b} = 0$ , where dislocation arrays (lines) that exhibit a loss of contrast (the disappearance of the leading partials, discussed below) are most probably associated with defects formed in the  $\epsilon$ -Ge epilayers. Therefore, some TDDs or MDs most probably exist within the  $\epsilon$ -Ge epilayer. The individual MDs that form in the  $\epsilon$ -Ge epilayer would likely not have sufficient time or energy to glide and therefore form the neat MD arrays that we see in the PV-TEM images, if the epilayer remains mostly strained, as is the case here.

**Invisibility Criterion for Disassociated Misfit Dislocations under Plan-View TEM Imaging.** A complete Burgers vector analysis by the invisibility criterion  $\mathbf{g} \cdot \mathbf{b} = 0$  was difficult. This is largely due to the inability to maintain a constant  $\mathbf{g}$  vector over a sufficiently large region in a bent specimen foil. Moving to thicker regions where bending was minimized was not effective since these extremely thick regions give a substantial dynamical diffraction contrast due to the diffracted beam being rediffracted multiple times, weakening the two-beam condition during measurement. However, in a moderately thick region ( $\sim 400 \text{ nm}$ ), a constant low index  $\langle 220 \rangle$  type  $\mathbf{g}$  vector could be obtained over a small area, a few  $\mu\text{m}^2$ , as shown in Figure 8a. Working within these limitations, we observed that MD lines parallel to the  $\mathbf{g}$  vector at the  $\epsilon$ -Ge/InGaAs interface retain significant residual contrast. This is shown in Figure 8a,b and is also examined quantitatively in Figure 9, which is a magnification of the image given in Figure 8a. Dislocation lines in the 0.7%  $\epsilon$ -Ge sample parallel to a  $\langle 220 \rangle$  type  $\mathbf{g}$  vector provided  $\sim 40\%$  less contrast than lines perpendicular to  $\mathbf{g}$ , as measured in Figure 9. As previously discussed, the MDs are expected to be disassociated in perfect  $60^\circ$  dislocations, with the separation distance between the SPDs being constrained by the 15 nm height of the  $\epsilon$ -Ge film. A  $60^\circ$  dislocation with its line directed along the  $[\bar{1}01]$  direction, as shown in Figure 8a, with Burgers vector  $\mathbf{b} = \frac{1}{2}[\bar{1}01]$  will disassociate into a leading  $90^\circ$  SPD with  $\mathbf{b} = \frac{1}{6}[\bar{1}\bar{1}2]$  and a trailing  $30^\circ$  partial with  $\mathbf{b} = \frac{1}{6}[\bar{2}11]$ . If  $\mathbf{g}$  is set to  $[2\bar{2}0]$  as in Figure 8a, the leading pure-edge dislocation should vanish since both  $\mathbf{g} \cdot \mathbf{b}$  and  $\mathbf{g} \cdot (\mathbf{b} \times \mathbf{u})$  are both equal to zero, where  $\mathbf{u}$  is a unit vector parallel to the dislocation line.<sup>46</sup> However, the trailing  $30^\circ$  partial will not lose contrast since  $\mathbf{g} \cdot \mathbf{b} = -1$ . At the scale of the image in Figure 8a, the contrast caused by the leading and trailing dislocations virtually overlapping is due to the narrow separation of the partials. Therefore, when the leading partial loses contrast due to the diffraction condition, we should still see a dislocation line due to the trailing partial, but the total contrast should be measurably reduced. This behavior is exactly what we have observed here. The loss of contrast appears to occur primarily on one side of the dislocation line, reflecting the nonzero separation distance between the leading (invisible) and trailing

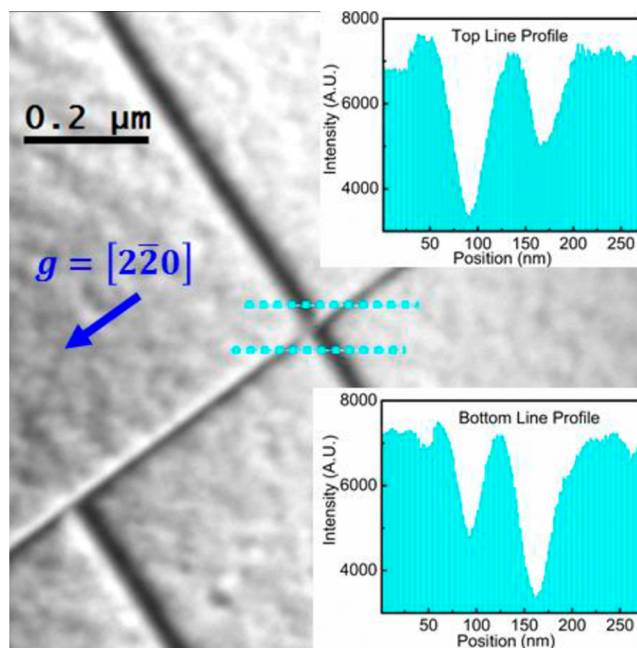


**Figure 9.** Quantitative contrast analysis of two orthogonal MDs. The dotted blue lines represent histogram line profiles of the intensity from the dislocation intersection shown in the top right of Figure 8a. The dislocation parallel to  $\mathbf{g}$  has measurably reduced contrast.

(visible) partials. Upon analyzing the detailed formation of MDs and their interactions, we can conclude that the defect density is in the well-controlled range of mismatch epitaxy,<sup>46</sup> and the room-temperature photoluminescence properties are another important benchmarking property for tensile-strained Ge, as discussed below.

**Room-Temperature Photoluminescence Properties of Direct Band Gap 1.6%  $\epsilon$ -Ge.** An important design parameter considered for the  $\epsilon$ -Ge-based laser structure is the optical cladding material surrounding the direct band gap Ge. The cladding material should provide both carrier and optical confinement in the  $\epsilon$ -Ge layer, with minimal-to-negligible absorption. This cladding material should also permit light emission from the lasing media,  $\epsilon$ -Ge,<sup>31,35,38–40</sup> through the thinner upper barrier. The thickness and composition are also important such that the refractive indices of the various layers are suitable for strong optical confinement as well as emission of the laser wavelength due to the modification of the band gap via strain engineering in Ge. Figure 10 shows the observed room-temperature photoluminescence (PL) intensities near the direct gap obtained from a 30 nm thick 1.6%  $\epsilon$ -Ge layer grown GaAs substrate using graded  $\text{In}_x\text{Ga}_{1-x}\text{As}$  metamorphic buffer as a function of excitation power varied from 6 to 23 W/cm<sup>2</sup> under 700 nm Ti:Sa pulsed excitation mode. The spectra were obtained using an InAs liquid nitrogen chilled detector. One can find from this figure that, with increasing laser power, the peak luminescence intensity is increasing, but the peak position remains at the same position. The lower-energy side of each PL spectrum is slightly steeper than the high-energy side. The direct band gap luminescence line shape is less influenced by reabsorption due to the limited 30 nm thickness of the Ge layer.<sup>54</sup> In addition, one can find from Figure 10 that the peak energy is at  $\sim 0.6609 \text{ eV}$ , which is the direct band gap transition from the conduction band at the  $\Gamma$ -valley to the heavy-hole (HH) transition and/or from the L-valley to the

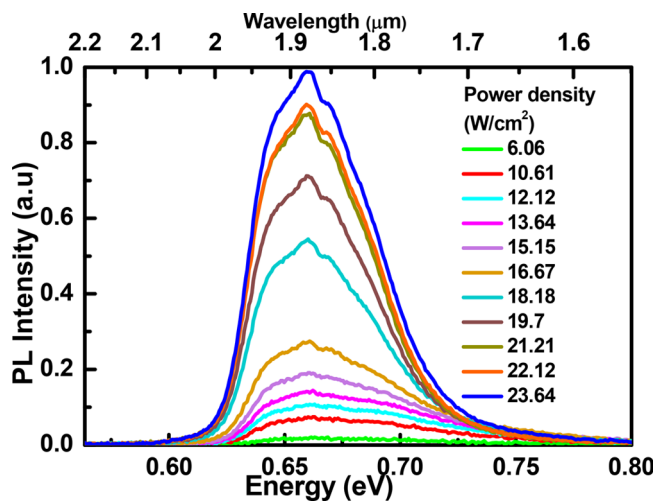


**Figure 10.** Room-temperature power dependent PL spectra of a 1.6% tensile-strained Ge layer on  $\text{In}_{0.24}\text{Ga}_{0.76}\text{As}/\text{In}_x\text{Ga}_{1-x}\text{As}/\text{GaAs}$ , exhibiting the direct band gap recombination.

HH transition. From Figure 1b, one can find that the energy levels of  $\Gamma$ - and L-valleys are almost the same, and the L-valley will still retain the majority of excited electrons. For the minimum excitation power density of  $6.06 \text{ W/cm}^2$ , it is likely that minimal recombination was detectable due to insufficient filling of  $\Gamma$ -valley states as compared to the majorly filled L-valley states. At higher excitation power density at this 1.6% strain level or at higher tensile strain states (e.g., 1.96%), strain-induced splitting of the  $\Gamma$ - and L-valley conduction band (CB) minima results in a significantly lower  $\Gamma$ -valley CB minimum; hence, the direct band gap optical transition from the Ge is possible. The peak energy position for this 1.6% tensile-strained Ge at 300 K is in agreement with the band gap versus misfit strain relation reported by Guiloy et al.<sup>55</sup> and Suess et al.<sup>56</sup> for Ge microbridges by photoreflectance spectroscopy at room temperature. It also agrees with the calculated optical gain versus photon energy shown in Figure 6b. In most of the literature,<sup>30,31,40,44</sup> the PL spectra were recorded from tensile-strained Ge grown on III–V buffers with a low-temperature measurement, and this result is the first room-temperature PL spectra obtained from the 1.6% biaxially strained Ge grown on InGaAs buffer. Moreover, this  $\text{Ge}/\text{In}_{0.24}\text{Ga}_{0.76}\text{As}$  sample revealed strong Fabry–Perot (FP) oscillations at the maximum of the gain curve. One can find that the emission wavelength is centered at about  $1.9 \mu\text{m}$  (Figure 10) and has a wavelength span within a full width at half-maximum of  $\sim 150 \text{ nm}$ . Once the strain amount inside the Ge is above 1.5%, the L-valley and  $\Gamma$ -valley are at the same conduction band minimum (see Figure 1b), and hence, the material is direct band gap, as reported by our earlier work<sup>31,35,38–40</sup> and by others.<sup>27,55,56</sup> Beyond the tensile-strained amount of 1.5%, the optical transition must be from the conduction band at the  $\Gamma$ -valley to LH or HH. The optical transition from the  $\Gamma$ -valley to LH is also evident.<sup>40</sup> Since the densities of states are small in the LH band compared with the HH band due to lower effective mass when separated by strain, one can expect the optical transition from the conduction band at the  $\Gamma$ -valley to the HH despite the fact that the LH band is above the HH band, as shown in Figure 1. The carriers generated during higher optical excitation at the  $\Gamma$ -valley would not transfer to the L-valley due to the steeper curvature of the  $\Gamma$ -valley as compared to that of the L-valley. The  $\Gamma$ -valley states will be deeply

populated as more carriers are injected by optical pumping.<sup>21,24,57–59</sup> It has been reported that the percentage of carrier population in the  $\Gamma$ -valley increased with increasing optical excitation power.<sup>59</sup> One might assume that the indirect-to-direct crossover point might vary depending on the amount of tensile strain in Ge, and indeed, several works in the literature reported the indirect-to-direct crossover point in the range 1.5–2% tensile strained in Ge.<sup>40,55,56</sup> This makes an ambiguity whether the optical transition is indeed solely from the conduction band at the  $\Gamma$ -valley, not from the L-valley. In order to confirm the optical transition, we have plotted the peak energy as well as integrated PL intensity as a function of excitation power. Figure 11a shows the peak energy obtained

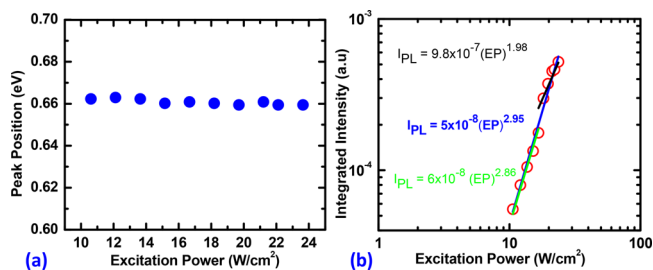


**Figure 11.** (a) Peak position as a function of excitation power and (b) integrated peak intensity with excitation power.

from Figure 10 as a function of excitation power density. One can find that the peak position remains constant with laser excitation power studied in this work, which is in agreement with the room-temperature steady state recombination modeling results<sup>59</sup> for biaxial tensile-strained Ge with various strain levels from 0% to 2.5%. This further confirms the direct band gap of Ge and that the optical transition is from the  $\Gamma$ -valley due to the higher radiative recombination rate.

It has been widely reported that the laser power dependence on the near band edge PL can provide the nature of optical transition in semiconductors and their heterostructures.<sup>27,60–62</sup> Figure 11b shows the integrated PL intensity ( $I_{\text{PL}}$ ) obtained from Figure 10 as a function of excitation power. One can find that the luminescence intensity increases with excitation power. The  $I_{\text{PL}}$  is related to the excitation intensity through the relation  $I_{\text{PL}} = CP^k$ , where  $C$  is a constant,  $P$  is the excitation power density, and  $k$  is the power factor.<sup>61</sup> It has been reported that the  $k < 2$  is for indirect transition (e.g., L-to-HH) and  $k = 2$  for the direct transition ( $\Gamma$ -to-HH) for Ge, since the PL intensity is proportional to the number of electrons and holes taking place during the recombination process. From Figure 11b, one can find that the integrated luminescence intensity varies superlinearly with excitation power, which is in agreement with the reported results by Jain et al.,<sup>59</sup> Klingenstein and Schweizer,<sup>54</sup> and Arguirov et al.<sup>62</sup> for strained and unstrained Ge, respectively. The  $k$  values were obtained in the range 1.98–2.95 depending on the data set used during the fitting process. The extracted  $k$  value is 2 or well above 2. The power factor of  $k = 2.4$  was reported by Jain et al.<sup>59</sup> for 0.82% biaxially tensile-strained Ge using steady-state recombination modeling and  $k = 6.4$  experimentally. Therefore, we can conclude that the PL spectra obtained here are from the direct transition in the conduction band at the  $\Gamma$ -valley, and due to higher excitation, the direct recombination will occur significantly as compared to the nonradiative recombination via defects or dislocations. Figure 12 is a zoom-in emission

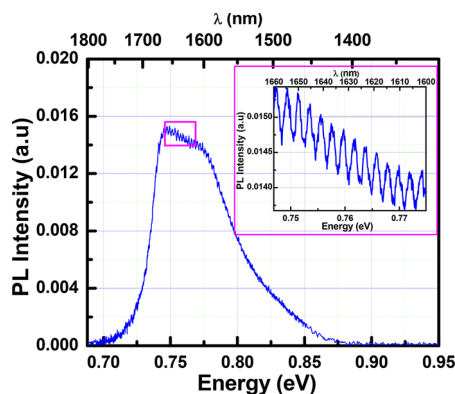


**Figure 12.** Room-temperature PL spectrum of a 1.6% tensile-strained Ge layer on  $\text{In}_{0.24}\text{Ga}_{0.76}\text{As}/\text{In}_x\text{Ga}_{1-x}\text{As}/\text{GaAs}$  measured using a high-gain InGaAs detector, displaying Fabry–Perot oscillation. The inset shows the zoom-in spectrum from the FP oscillation section.

spectrum measured with a high-gain InGaAs detector, which is sensitive below  $1.7 \mu\text{m}$ . One can find from this figure the visible Fabry–Perot oscillation on the top of the PL spectrum. This signifies the quality of strained Ge material synthesis via MBE and its Ge/InGaAs heterointerface.

**Strain Analysis of the  $\epsilon\text{-Ge}/\text{In}_x\text{Ga}_{1-x}\text{As}$  QW Heterostructure via X-ray Diffraction.** Utilizing the design by the FIMMWAVE mode solver of the  $\epsilon\text{-Ge}$  QW laser structure, as shown in Figure 2, we have grown the  $\epsilon\text{-Ge}$  QW laser structure on GaAs substrate using an interconnected dual chamber solid source MBE system. To determine the structural quality and relaxation state of the Ge QW laser structure, reciprocal space maps (RSMs), of symmetric (004) and asymmetric (115), were recorded during the X-ray measurement from this structure. Figure 13a,b shows (004)

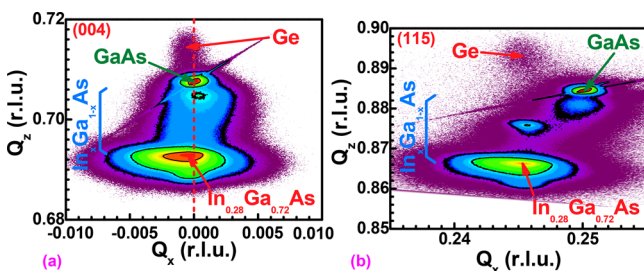


**Figure 13.** X-ray reciprocal space maps of (a) (004) symmetric and (b) (115) asymmetric scan from the  $\text{In}_{0.28}\text{Ga}_{0.72}\text{As}/\epsilon\text{-Ge}/\text{In}_{0.28}\text{Ga}_{0.72}\text{As}$  QW laser structure on GaAs substrate, respectively. All of these results demonstrated the strained  $\epsilon\text{-Ge}$  QW. The Ge is almost fully strained as indicated by the strained line shown in part a as well as the peak location of the Ge with respect to the GaAs substrate. Also, the RLP of Ge lies on the top of the RLP of constant composition  $\text{In}_{0.28}\text{Ga}_{0.72}\text{As}$  layer, confirming the  $\epsilon\text{-Ge}$ .

symmetric and (115) asymmetric RSMs, respectively, for this structure. Using the measured perpendicular and parallel lattice constants, we have determined the In composition in the constant composition upper InGaAs layer. We have found that the targeted 13 nm  $\epsilon\text{-Ge}$  QW layer is tensile strained with respect to the constant composition of the  $\text{In}_{0.28}\text{Ga}_{0.72}\text{As}$  confinement layer that has provided a  $\sim 1.95\%$  amount of the tensile-strained Ge QW layer. In this laser structure, a  $2.0 \mu\text{m}$  upper  $\text{In}_{0.28}\text{Ga}_{0.72}\text{As}$  barrier layer (same thickness as the bottom  $\text{In}_{0.28}\text{Ga}_{0.72}\text{As}$  barrier layer) was selected for carrier and

optical confinement in the  $\epsilon\text{-Ge}$  QW. In the  $\text{In}_x\text{Ga}_{1-x}\text{As}$  linearly graded buffer, we have selected an In overshoot composition of  $\sim 30\%$  ( $\sim 100 \text{ nm}$  thickness) in order to fully relax the buffer layer when grown on GaAs substrate. The reciprocal lattice point (RLP) of Ge,  $\text{In}_{0.28}\text{Ga}_{0.72}\text{As}$ , graded InGaAs, and GaAs substrate is clearly visible in Figure 13a,b. One can find from (004) RSM that the  $\epsilon\text{-Ge}$  layer is indeed tensile strained since the RLP of  $\epsilon\text{-Ge}$  is located on the top RLP of the GaAs substrate, and the small contour below the RLP of the  $\text{In}_{0.28}\text{Ga}_{0.72}\text{As}$  layer is the RSM of the overshoot  $\text{In}_{0.30}\text{Ga}_{0.70}\text{As}$  layer (the small hump below label  $\text{In}_{0.28}\text{Ga}_{0.72}\text{As}$ ). The lowered growth temperature of  $450 \text{ }^\circ\text{C}$  compared to the bottom InGaAs layer growth temperature ( $525 \text{ }^\circ\text{C}$ ) was selected for the upper  $\text{In}_{0.28}\text{Ga}_{0.72}\text{As}$  layer growth on the top of the 13 nm  $\epsilon\text{-Ge}$  QW layer, just to make sure that the strain inside the 13 nm  $\epsilon\text{-Ge}$  QW layer would not relax during the growth of the upper  $2 \mu\text{m}$   $\text{In}_{0.28}\text{Ga}_{0.72}\text{As}$  layer. Whether the upper  $\text{In}_x\text{Ga}_{1-x}\text{As}$  layer is relaxed or lattice matched with the in-plane lattice constant of  $\epsilon\text{-Ge}$  QW, cross-sectional TEM microscopic analysis is essential. If the composition of the upper  $\text{In}_x\text{Ga}_{1-x}\text{As}$  layer is different during growth on top of  $\epsilon\text{-Ge}$ , one should expect the RLP of that InGaAs layer beside the RLP of the constant composition bottom  $\text{In}_{0.28}\text{Ga}_{0.72}\text{As}$  layer. Since there was no visible separate RLP of the constant composition InGaAs layer from the bottom and top layer, we can ensure that the upper In composition in the InGaAs layer is almost identical to the bottom constant In composition of InGaAs. However, the broadness of the InGaAs contour is due to lattice constant distortions, i.e., defect-induced broadening. By examining the cross-sectional TEM analysis of the structure, discussed below, we can infer that the lattice distortion broadening is due to the upper InGaAs layer. To further verify this point, the thickness of the upper InGaAs epilayer is large ( $2.0 \mu\text{m}$ ) compared to the overshoot layer within the metamorphic buffer (less than  $100 \text{ nm}$ ). Accordingly, it should have a larger Bragg diffraction intensity. Due to this, it is possible that a portion of the lattice contour intensity between the primary InGaAs centroid (labeled, Figure 13a) and the overshoot layer centroid (the small, green “hump” in Figure 13a) is due to the upper InGaAs layer if the upper InGaAs layer were to have a larger lattice constant than the lower InGaAs layer. Explicitly, this would indicate that the upper InGaAs layer has a higher In composition than the lower InGaAs layer and, thus, the lattice mismatch-induced defect formation in the upper InGaAs layer. This claim could be further supported by the absence of an additional diffraction centroid at a higher  $Q_z$  (lower lattice constant, lower In composition) than the main InGaAs centroid (labeled, Figure 13a). By considering the HR-XRD and cross-sectional TEM data together, we believe that the measured In composition more accurately reflects that of the lower InGaAs layer, whereas the upper InGaAs layer likely has a higher lattice constant (In composition) and was therefore found to be defective due to the lattice mismatch (evident in the cross-sectional TEM images below). Because of the defect-associated distortion to the upper InGaAs diffraction contour, and its relatively high intensity, the upper InGaAs diffraction contour exists as a “smear” between the labeled, lower InGaAs centroid and the unlabeled overshoot layer centroid. Thus, the referred RLP of the  $\text{In}_{0.28}\text{Ga}_{0.72}\text{As}$  layer, as shown in Figure 13a,b, is the signal from both bottom and top  $\text{In}_x\text{Ga}_{1-x}\text{As}$  layers. Therefore, RSMs of our  $1.95\%$   $\epsilon\text{-Ge}$  QW laser structure on GaAs with top  $\text{In}_x\text{Ga}_{1-x}\text{As}$  ( $0.28 < x < 0.30$ ) and bottom

$\text{In}_{0.28}\text{Ga}_{0.72}\text{As}$  barrier layers demonstrated the quasi-pseudomorphic nature of the  $\epsilon\text{-Ge}$  layer, where the  $\epsilon\text{-Ge}$  lattice constant is in agreement with the in-plane lattice constant of the  $\text{In}_{0.28}\text{Ga}_{0.72}\text{As}$  bottom barrier layer.

**Defect Analysis of  $\epsilon\text{-Ge}/\text{In}_x\text{Ga}_{1-x}\text{As}$  QW Heterostructures via Cross-Sectional TEM.** In addition to the X-ray analysis above, cross-sectional TEM analysis of the  $\epsilon\text{-Ge}$  QW laser structure is indispensable. The cross-sectional TEM micrographs of our 1.95%  $\epsilon\text{-Ge}$  QW laser structure on GaAs with InGaAs barrier layers are shown in Figure 14. The low- and

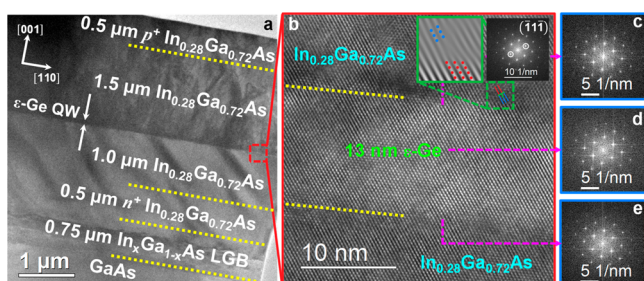


**Figure 14.** (a) Cross-sectional TEM of the entire laser structure. (b) HR-TEM view of the  $\text{In}_{0.28}\text{Ga}_{0.72}\text{As}/\epsilon\text{-Ge}/\text{In}_{0.28}\text{Ga}_{0.72}\text{As}$  QW part. (c–e) FFT patterns from the upper  $\text{In}_{0.28}\text{Ga}_{0.72}\text{As}/\epsilon\text{-Ge}$ ,  $\epsilon\text{-Ge}$ ,  $\epsilon\text{-Ge}/\text{In}_{0.28}\text{Ga}_{0.72}\text{As}$  heterointerface region, respectively. All of these results demonstrated the strained  $\epsilon\text{-Ge}$  QW.

high-magnification TEM micrographs, shown in Figure 14a,b, corresponding to the entire  $\epsilon\text{-Ge}$  laser structure and the  $\epsilon\text{-Ge}/\text{In}_{0.28}\text{Ga}_{0.72}\text{As}$  heterointerface, respectively, highlight the confinement of lattice mismatch-induced defects below the region of interest. As can be seen from Figure 14a, the linearly graded  $\text{In}_x\text{Ga}_{1-x}\text{As}$  buffer accommodated the misfit strain via the formation and subsequent glide of threading dislocations, thereby preventing substantial defect propagation along the growth direction. Correspondingly, the constant-composition  $\text{In}_{0.28}\text{Ga}_{0.72}\text{As}$  stressor was observed to be absent of long-range microstructural defects or disorder, implicitly supporting the high degree of relaxation and crystallinity found via the X-ray analysis above. Examining Figure 14b, one can find that the epitaxial  $\epsilon\text{-Ge}$  and the constant composition  $\text{In}_{0.28}\text{Ga}_{0.72}\text{As}$  stressor exhibited a highly uniform heterointerface. Atom probe tomography study demonstrated a 6 Å heterointerface abruptness of the  $\text{Ge}/\text{In}_{0.24}\text{Ga}_{0.76}\text{As}$  heterostructure (not shown here). The lattice indexing shows the lattice line extending from the  $\epsilon\text{-Ge}$  layer to the  $\text{In}_{0.28}\text{Ga}_{0.72}\text{As}$  layer, and it also shows that the Ge in-plane lattice constant internally matches with the lattice constant of the  $\text{In}_{0.28}\text{Ga}_{0.72}\text{As}$  bottom layer, demonstrating the tensile strain  $\epsilon\text{-Ge}$ , which is also supported by the X-ray analysis above (Figure 13).

As we have demonstrated with the tensile-strained Ge on the bottom  $\text{In}_{0.28}\text{Ga}_{0.72}\text{As}$  layer, the fast-Fourier transform (FFT) patterns were taken from the top  $\text{In}_{0.28}\text{Ga}_{0.72}\text{As}/\epsilon\text{-Ge}$  heterointerface,  $\epsilon\text{-Ge}$ , and  $\epsilon\text{-Ge}/\text{In}_{0.28}\text{Ga}_{0.72}\text{As}$  heterointerface, and the results are shown in Figure 14c–e, respectively. These results suggest an atomically abrupt heterointerface of lacking visible atomic interdiffusion or relaxation-inducing misfit dislocations (MDs). The absence of satellite reflections in Figure 13c–e confirms a single lattice constant (i.e.,  $a_{\text{In}_{0.28}\text{Ga}_{0.72}\text{As}} = a_{\text{Ge}}$ ) to the diffractogram, thereby providing additional support for a quasi-ideal pseudomorphic Ge epitaxy, where the  $\epsilon\text{-Ge}$  lattice constant matches with the in-plane lattice constant of the  $\text{In}_{0.28}\text{Ga}_{0.72}\text{As}$  bottom and upper barrier layers. In

addition, the inverse FFT patterns were taken from both the top  $\text{In}_{0.28}\text{Ga}_{0.72}\text{As}/\epsilon\text{-Ge}$  heterointerface and the  $\text{In}_{0.28}\text{Ga}_{0.72}\text{As}/\epsilon\text{-Ge}/\text{In}_{0.28}\text{Ga}_{0.72}\text{As}$  QW part to identify if there are any MDs present in the top or bottom heterointerface. The reconstructed HR-TEM micrograph from the top  $\text{In}_{0.28}\text{Ga}_{0.72}\text{As}/\epsilon\text{-Ge}$  heterointerface shown in Figure 14b is used to identify the lattice lines at the interface and hence to identify the types of dislocations present at the heterointerface. Figure 15 shows the

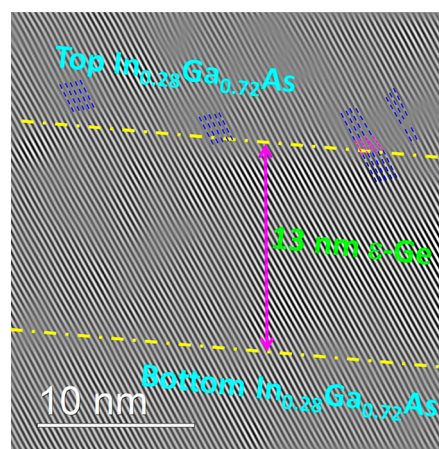


**Figure 15.** Filtered FFT pattern of the  $\text{In}_{0.28}\text{Ga}_{0.72}\text{As}/\epsilon\text{-Ge}/\text{In}_{0.28}\text{Ga}_{0.72}\text{As}$  QW laser structure, showing the misfit dislocations only in the upper  $\text{In}_{0.28}\text{Ga}_{0.72}\text{As}$  layer.

inverse FFT pattern taken from the part of the  $\text{In}_{0.28}\text{Ga}_{0.72}\text{As}/\epsilon\text{-Ge}/\text{In}_{0.28}\text{Ga}_{0.72}\text{As}$  QW which shows the formation of MDs at the top  $\text{InGaAs}/\epsilon\text{-Ge}$  heterointerface. One can find that the MDs only appeared in the upper  $\text{In}_{0.28}\text{Ga}_{0.72}\text{As}$  layer as linear defects and are considered as an insertion of an extra half-plane of atoms (see the blue–pink region), and none were present at the bottom heterointerface. This would suggest that there is some degree of lattice mismatch at this interface that resulted in defect formation and strain relaxation. The fact that these MDs are absent at the bottom  $\epsilon\text{-Ge}/\text{InGaAs}$  heterointerface suggests that, on the other hand, the bottom heterointerface is perfectly lattice matched. Moreover, the thick 2  $\mu\text{m}$   $\text{In}_{0.28}\text{Ga}_{0.72}\text{As}$  upper barrier layer minimizes the relaxation of the entire  $\epsilon\text{-Ge}$  lasing media of 13 nm, which is needed for a fixed wavelength light emission.

## CONCLUSIONS

We have demonstrated the strain and band gap engineered epitaxial  $\epsilon\text{-Ge}$  layers as well as  $\epsilon\text{-Ge}$  quantum-well laser structures through theoretical calculations and experimentally. The biaxial tensile strain in the range 0.7–1.96% in the  $\epsilon\text{-Ge}$  layer was provided by the InGaAs stressor during material synthesis using molecular beam epitaxy for optical and carrier confinement. The simulated direct band-to-band gain, threshold current density, and loss mechanisms that dominate the  $\epsilon\text{-Ge}$  QW laser structure were calculated. It has been shown that the higher strain increases the gain at higher wavelengths and at lower injection concentrations; however, the decreasing  $\epsilon\text{-Ge}$  QW thicknesses are needed for higher strains to avoid strain relaxation. In addition, the  $J_{\text{th}}$  can be greatly reduced from 300  $\text{A}/\text{cm}^2$  at 0.2% strain to  $<10$   $\text{A}/\text{cm}^2$  at 1.96% strain level. The room-temperature PL measurement demonstrated direct band gap optical emission from the conduction band at the  $\Gamma$ -valley to HH (0.6609 eV) from the 1.6% strained Ge/

In<sub>0.24</sub>Ga<sub>0.76</sub>As heterostructure. The threading dislocation density is below  $4 \times 10^6 \text{ cm}^{-2}$  for 1.2%  $\epsilon$ -Ge, which is an upper bound, exhibiting superior material quality. X-ray and transmission electron microscopy analysis of the experimentally realistic 1.95% biaxially strained In<sub>0.28</sub>Ga<sub>0.72</sub>As/13 nm  $\epsilon$ -Ge/In<sub>0.28</sub>Ga<sub>0.72</sub>As QW laser structure demonstrated coherent epitaxy of  $\epsilon$ -Ge on In<sub>0.28</sub>Ga<sub>0.72</sub>As barrier layers and minimal relaxation of the Ge layer. Therefore, our strain and band gap engineered  $\epsilon$ -Ge on GaAs and ultimately the transfer of the process to the Si substrate using III–V metamorphic buffer would provide a major step toward the integration of Ge-based photonic devices on Si.

## MATERIALS AND METHODS

**Electronic Structure Calculation.** The calculations of the gain  $G$  and current density  $J$  are dependent on states of the whole Brillouin zone: the optical transitions occur around the direct gap at  $\Gamma$ , while the density of states, carrier density, and chemical potential have a larger dependence on the conduction band near the L-valley. The electronic band structure across the whole Brillouin zone was calculated using the 30-band k-p approach of refs 63 and 64. The quantization condition was calculated using the “Truncated Crystal Approximation”<sup>65</sup> by considering the  $k$ -points in each valley that are compatible with the boundary conditions given by the thickness of the QW assuming hard wall boundaries. We justify the use of hard wall boundaries, rather than a more exact softer approach such as that of ref 66, by the strong type I nature of the offset between the Ge and InGaAs layer, with  $\Gamma$  and L respective band offsets of 0.5 and close to 1 eV. This approximation allows us to calculate the quantized subbands across the whole Brillouin zone with the parameters of the Ge layer only, without the need for iterations including the InGaAs layer. The detailed methodology of the electronic structure calculations was discussed in the Results and Discussion section. All parameters of the strained Ge band structure can be found in ref 63.

**Material Synthesis.** The epitaxial strained Ge layers in the thickness range 13–75 nm and Ge quantum-well laser structure was grown on semi-insulating (100)/2° GaAs substrates. Vacuum interconnected solid source molecular beam epitaxy growth chambers, one for Ge and another for III–V materials, were used for material synthesis. The growth temperature and growth rate of epitaxial Ge were 400 °C and 0.1 Å/s, respectively. In brief, the GaAs oxide desorption was taken at 750 °C, measured by a thermocouple, under arsenic overpressure of  $\sim 10^{-5}$  Torr. After the oxide desorption, the 250 nm thick undoped GaAs was grown at 650 °C prior to the linearly graded In<sub>x</sub>Ga<sub>1-x</sub>As metamorphic buffer layer to a targeted In composition of 0.28 for the 1.95% strained Ge QW structure. Within the 0.75  $\mu\text{m}$  thick In<sub>x</sub>Ga<sub>1-x</sub>As linearly graded buffer, a 100 nm thick In<sub>0.30</sub>Ga<sub>0.70</sub>As layer was inserted in order for the faster relaxation of the InGaAs graded buffer layer for acting as virtual substrate. The bottom barrier In<sub>0.28</sub>Ga<sub>0.72</sub>As layer thickness of 1.5  $\mu\text{m}$  was grown prior to the 13 nm Ge layer growth on top of this constant composition In<sub>0.28</sub>Ga<sub>0.72</sub>As layer, which act as a bottom barrier layer. Note that the sample was vacuum transferred to the Ge MBE chamber for Ge layer growth and then back to the III–V MBE chamber for upper 2.0  $\mu\text{m}$  thick InGaAs layer growth. The growth temperatures of the bottom and upper InGaAs layer were 525 and 450 °C, and the growth rate was fixed at 0.7  $\mu\text{m}/\text{h}$ , respectively. The details of the growth procedure are reported elsewhere.<sup>31,35,38</sup>

**Materials Characterization.** High-resolution X-ray diffraction measurements using a Panalytical MRD Pro instrument with PIXcel and triple axis detection capability were recorded for a determination of the structural quality and the relaxation state of epitaxial Ge layers. Cross-sectional and plan-view transmission electron microscopy analyses were performed to determine the entire laser structure and defect density within the strained Ge layers. The HR-TEM imaging was performed using a TITAN transmission electron microscope, and image processing was performed using Gatan image filtering software. For this purpose, the electron transparent foil of the thin film cross-

section and plan-view of the selective strained Ge and laser structure were prepared by a standard polishing technique. The PV-TEM imaging was performed using a JEOL 2100 transmission electron microscope. Room-temperature photoluminescence measurements were performed to determine the band gap of tensile-strained Ge using a Ti:Sa pulsed laser as a source of excitation with a variable excitation intensity, as indicated in Figure 8. Both liquid nitrogen cooled InGaAs and InAs detectors were used to collect the signal from the sample. The details of the measurement setup and procedure of collecting data from the sample surface were recently reported.<sup>40</sup>

## AUTHOR INFORMATION

### Corresponding Author

Mantu K. Hudait – Advanced Devices & Sustainable Energy Laboratory (ADSEL), Bradley Department of Electrical and Computer Engineering, Virginia Tech, Blacksburg, Virginia 24061, United States; [orcid.org/0000-0002-9789-3081](https://orcid.org/0000-0002-9789-3081); Phone: (540) 231-6663; Email: [mantu.hudait@vt.edu](mailto:mantu.hudait@vt.edu); Fax: (540) 231-3362

### Authors

Felipe Murphy-Armando – Tyndall National Institute, Lee Maltings, Cork T12 R5CP, Republic of Ireland

Dzianis Saladukha – The Centre for Advanced Photonics & Process Analysis, Munster Technological University at Tyndall National Institute, Cork T12R5CP, Republic of Ireland

Michael B. Clavel – Advanced Devices & Sustainable Energy Laboratory (ADSEL), Bradley Department of Electrical and Computer Engineering, Virginia Tech, Blacksburg, Virginia 24061, United States; [orcid.org/0000-0002-2925-6099](https://orcid.org/0000-0002-2925-6099)

Patrick S. Goley – Advanced Devices & Sustainable Energy Laboratory (ADSEL), Bradley Department of Electrical and Computer Engineering, Virginia Tech, Blacksburg, Virginia 24061, United States

Deepam Maurya – Center for Energy Harvesting Materials and Systems (CEHMS), Mechanical Engineering, Virginia Tech, Blacksburg, Virginia 24061, United States

Shuvodip Bhattacharya – Advanced Devices & Sustainable Energy Laboratory (ADSEL), Bradley Department of Electrical and Computer Engineering, Virginia Tech, Blacksburg, Virginia 24061, United States

Tomasz J. Ochalski – The Centre for Advanced Photonics & Process Analysis, Munster Technological University at Tyndall National Institute, Cork T12R5CP, Republic of Ireland

Complete contact information is available at:

<https://pubs.acs.org/10.1021/acsaelm.1c00660>

### Notes

The authors declare no competing financial interest.

## ACKNOWLEDGMENTS

M.B.C. and M.K.H. acknowledge partial support from the NSF under grant number ECCS-1507950 and ECCS-2042079, a US–Ireland joint R&D program. Authors acknowledge NCFI-Institute for Critical Technology and Applied Science and Virginia Tech Nanofabrication facilities for materials characterization. The authors also acknowledge Dr. Luke F. Lester for several insightful technical discussions related to this work. F.M.-A. acknowledges Science Foundation Ireland grants SFI/14/US/I3057, 17/QERA/3473, and 19/FFP/6953.

## REFERENCES

- (1) Chow, W. W. Model for direct-transition gain in a Ge-on-Si laser. *Appl. Phys. Lett.* **2012**, *100*, 191113.
- (2) Elbaz, A.; Buca, D.; von den Driesch, N.; Pantzas, K.; Patriarche, G.; Zerounian, N.; Herth, E.; Checoury, X.; Sauvage, S.; Sagnes, J.; Foti, A.; Ossikovski, R.; Hartmann, J.-M.; Boeuf, F.; Ikonik, Z.; Boucaud, P.; Grützmacher, D.; El Kurdi, M. Ultra-low-threshold continuous-wave and pulsed lasing in tensile-strained GeSn alloys. *Nat. Photonics* **2020**, *14*, 375–382.
- (3) Soref, R. A.; Buca, D.; Yu, S.-Q. Group IV photonics-driving integrated optoelectronics. *Opt. Photonics News* **2016**, *27*, 32–39.
- (4) Stange, D.; Wirths, S.; Geiger, R.; Schulte-Braucks, C.; Marzban, B.; von den Driesch, N.; Mussler, G.; Zabel, T.; Stoica, T.; Hartmann, J.-M.; Mantl, S.; Ikonik, Z.; Grützmacher, D.; Sigg, H.; Witzens, J.; Buca, D. Optically Pumped GeSn Microdisk Lasers on Si. *ACS Photonics* **2016**, *3*, 1279–1285.
- (5) Al-Kabi, S.; Amir Ghetmiri, S. d.; Margetis, J.; Pham, T.; Zhou, Y.; Dou, W.; Collier, B.; Quinde, R.; Du, W.; Mosleh, A.; Liu, J.; Sun, G.; Soref, R. A.; Tolle, J.; Li, B.; Mortazavi, M.; Naseem, H. A.; Yu, S.-Q. An optically pumped 2.5  $\mu\text{m}$  GeSn laser on Si operating at 110 K. *Appl. Phys. Lett.* **2016**, *109*, 171105.
- (6) Singh, V.; Lin, P. T.; Patel, N.; Lin, H.; Li, L.; Zou, Y.; Deng, F.; Ni, C.; Hu, J.; Giammarco, J.; Paola Soliani, A.; Zdyrko, B.; Luzinov, I.; Novak, S.; Novak, J.; Wachtel, P.; Danto, S.; Musgraves, J. D.; Richardson, K.; Kimerling, L. C.; Agarwal, A. M. Mid-infrared materials and devices on a Si platform for optical sensing. *Sci. Technol. Adv. Mater.* **2014**, *15*, 2–14.
- (7) Zhou, Y.; Dou, W.; Du, W.; Ojo, S.; Tran, H.; Ghetmiri, S. A.; Liu, J.; Sun, G.; Soref, R.; Margetis, J.; Tolle, J.; Li, B.; Chen, Z.; Mortazavi, M.; Yu, S. – Q. Optically Pumped GeSn Lasers Operating at 270 K with Broad Waveguide Structures on Si. *ACS Photonics* **2019**, *6*, 1434–1441.
- (8) Bao, S.; Kim, D.; Onwukaeme, C.; Gupta, S.; Saraswat, K.; Lee, K. H.; Kim, Y.; Min, D.; Jung, Y.; Qiu, H.; Wang, H.; Fitzgerald, E. A.; Tan, C. S.; Nam, D. Low-threshold optically pumped lasing in highly strained germanium nanowires. *Nat. Commun.* **2017**, *8*, 1845.
- (9) von den Driesch, N.; Stange, D.; Wirths, S.; Mussler, G.; Holländer, B.; Ikonik, Z.; Hartmann, J. M.; Stoica, T.; Mantl, S.; Grützmacher, D.; Buca, D. Direct Bandgap Group IV Epitaxy on Si for Laser Applications. *Chem. Mater.* **2015**, *27*, 4693–4702.
- (10) Wang, Z.; Abbasi, A.; Dave, U.; De Groot, A.; Kumari, S.; Kunert, B.; Merckling, C.; Pantouvaki, M.; Shi, Y.; Tian, B.; Van Gasse, K.; Verbist, J.; Wang, R.; Xie, W.; Zhang, J.; Zhu, Y.; Bauwelinck, J.; Yin, X.; Hens, Z.; Van Campenhout, J.; Kuyken, B.; Baets, R.; Morthier, G.; Van Thourhout, D.; Roelkens, G. Novel Light Source Integration Approaches for Silicon Photonics. *Laser Photonics Rev.* **2017**, *11*, 1700063.
- (11) Seifried, M.; Villares, G.; Baumgartner, Y.; Hahn, H.; Halter, M.; Horst, F.; Caimi, D.; Caer, C.; Sousa, M.; Dangel, R. F.; Czornomaz, L.; Offrein, B. J. Monolithically Integrated CMOS-Compatible III–V on Silicon Lasers. *IEEE J. Sel. Top. Quantum Electron.* **2018**, *24*, 1–9.
- (12) Wang, H.; Kim, D.; Harfouche, M.; Santis, C. T.; Satyan, N.; Rakuljic, G.; Yariv, A. Narrow-Linewidth Oxide-Confined Heterogeneously Integrated Si/III–V Semiconductor Lasers. *IEEE Photonics Technol. Lett.* **2017**, *29*, 2199–2202.
- (13) Fadaly, E. M. T.; Dijkstra, A.; Suckert, J. R.; Ziss, D.; van Tilburg, M. A. J.; Mao, C.; Ren, Y.; van Lange, V. T.; Korzun, K.; Kölling, S.; Verheijen, M. A.; Busse, D.; Rödl, C.; Furthmüller, J.; Bechstedt, F.; Stangl, J.; Finley, J. J.; Botti, S.; Haverkort, J. E. M.; Bakkers, E. P. A. M. Direct-bandgap emission from hexagonal Ge and SiGe alloys. *Nature* **2020**, *580*, 205.
- (14) Nishizawa, N.; Kawagoe, H.; Yamanaka, M.; Matsushima, M.; Mori, K.; Kawabe, T. Wavelength Dependence of Ultrahigh-Resolution Optical Coherence Tomography Using Supercontinuum for Biomedical Imaging. *IEEE J. Sel. Top. Quantum Electron.* **2019**, *25*, 1–15.
- (15) Golovynskyi, S.; Golovynska, I.; Stepanova, L. I.; Datsenko, O. I.; Liu, L.; Qu, J.; Ohulchanskyy, T. Y. Optical windows for head tissues in near-infrared and short-wave infrared regions: Approaching transcranial light applications. *J. Biophotonics* **2018**, *11*, No. e201800141.
- (16) Zhu, B.; Kwon, S.; Rasmussen, J. C.; Litorja, M.; Sevic-Muraca, E. M. Comparison of NIR Versus SWIR Fluorescence Image Device Performance Using Working Standards Calibrated with SI Units. *IEEE Trans. Med. Imaging* **2020**, *39*, 944–951.
- (17) Wilson, R. H.; Nadeau, K. P.; Jaworski, F. B.; Tromberg, B. J.; Durkin, A. J. Review of short-wave infrared spectroscopy and imaging methods for biological tissue characterization. *J. Biomed. Opt.* **2015**, *20*, 030901.
- (18) Sun, C.; Wade, M. T.; Lee, Y.; Orcutt, J. S.; Alloatti, L.; Georgas, M. S.; Waterman, A. S.; Shainline, J. M.; Avizienis, R. R.; Lin, S.; Moss, B. R.; Kumar, R.; Pavanello, F.; Atabaki, A. H.; Cook, H. M.; Ou, A. J.; Leu, J. C.; Chen, Y. – H.; Asanović, K.; Ram, R. J.; Popović, M. A.; Stojanović, V. M. Single-chip microprocessor that communicates directly using light. *Nature* **2015**, *528*, 534.
- (19) Liang, D.; Bowers, J. E. Recent Progress in Lasers on Silicon. *Nat. Photonics* **2010**, *4*, 511–517.
- (20) Koshida, N.; Koyama, H. Visible Electroluminescence from Porous Silicon. *Appl. Phys. Lett.* **1992**, *60*, 347–349.
- (21) Cai, Y.; Han, Z.; Wang, X.; Camacho-Aguilera, R. E.; Kimerling, L. C.; Michel, J.; Liu, J. Analysis of Threshold Current Behavior for Bulk and Quantum-Well Germanium Laser Structures. *IEEE J. Sel. Top. Quantum Electron.* **2013**, *19*, 1901009.
- (22) Rong, H.; Liu, A.; Jones, R.; Cohen, O.; Hak, D.; Nicolaescu, R.; Fang, A.; Paniccia, M. An all-Silicon Raman Laser. *Nature* **2005**, *433*, 292–294.
- (23) Kuo, Y. H.; Lee, Y. K.; Ge, Y.; Ren, S.; Roth, J. E.; Kamins, T. I.; Miller, D. A. B.; Harris, J. S. Strong Quantum-Confined Stark Effect in Germanium Quantum-Well Structures on Silicon. *Nature* **2005**, *437*, 1334–1336.
- (24) Liu, J.; Sun, X.; Camacho-Aguilera, R.; Kimerling, L. C.; Michel, J. Ge-on-Si Laser Operating at Room Temperature. *Opt. Lett.* **2010**, *35*, 679–681.
- (25) El Kurdi, M.; Fishman, G.; Sauvage, S.; Boucaud, P. Band Structure and Optical Gain of Tensile-Strained Germanium Based on a 30 Band  $k\cdot p$  Formalism. *J. Appl. Phys.* **2010**, *107*, 013710.
- (26) Duan, G.-H.; Jany, C.; Le Liepvre, A.; Accard, A.; Lamponi, M.; Make, D.; Kaspar, P.; Levaufré, G.; Girard, N.; Lelarge, F.; Fedeli, J. M.; Messaoudene, S.; Bordel, D.; Olivier, S. Hybrid III-V on Silicon Lasers for Photonic Integrated Circuits on Silicon. *Proc. SPIE* **2014**, *9002*, 90020X-1–90020X-6.
- (27) Wada, K.; Kimerling, L. C. *Photonics and Electronics with Germanium*, 1st ed.; Wiley VCH, 2015.
- (28) Dutt, B. R.; Sukhdeo, D. S.; Nam, D.; Vulovic, B. M.; Yuan, Z.; Saraswat, K. C. Roadmap to an Efficient Germanium-on-Silicon Laser: Strain vs. n-type Doping. *IEEE Photonics J.* **2012**, *4*, 2002–2009.
- (29) Wirths, S.; Geiger, R.; von den Driesch, N.; Mussler, G.; Stoica, T.; Mantl, S.; Ikonik, Z.; Luysberg, M.; Chiussi, S.; Hartmann, J. M.; Sigg, H.; Faist, J.; Buca, D.; Grützmacher, D. Lasing in Direct-Bandgap GeSn Alloy Grown on Si. *Nat. Photonics* **2015**, *9*, 88–92.
- (30) Sanchez-Perez, J. R.; Boztug, C.; Chen, F.; Sudradjat, F. F.; Paskiewicz, D. M.; Jacobson, R. B.; Lagally, M. G.; Paiella, R. Direct-Bandgap Light-Emitting Germanium in Tensile Strained Nanomembranes. *Proc. Natl. Acad. Sci. U. S. A.* **2011**, *108*, 18893–18898.
- (31) Clavel, M.; Saladukha, D.; Goley, P.; Ochalski, T. J.; Murphy-Armando, F.; Bodnar, R. J.; Hudait, M. K. Heterogeneously-Grown Tunable Tensile Strained Germanium on Silicon for Photonic Devices. *ACS Appl. Mater. Interfaces* **2015**, *7*, 26470–26481.
- (32) Yang, J.; Bhattacharya, P.; Wu, Z. Monolithic Integration of InGaAs-GaAs Quantum-Dot Laser and Quantum-Well Electro-absorption Modulator on Silicon. *IEEE Photonics Technol. Lett.* **2007**, *19*, 747–749.
- (33) Groenert, M. E.; Leitz, C. W.; Pitera, A. J.; Yang, V.; Lee, H.; Ram, R. J.; Fitzgerald, E. A. Monolithic Integration of Room-temperature GaAs/AlGaAs Lasers on Si Substrates via Relaxed Graded GeSi Buffer Layers. *J. Appl. Phys.* **2003**, *93*, 362–367.

- (34) Liu, J. F.; Sun, X.; Pan, D.; Wang, X. X.; Kimerling, L. C.; Koch, T. L.; Michel, J. Tensile-Strained, n-type Ge as a Gain Medium for Monolithic Laser Integration on Si. *Opt. Express* **2007**, *15*, 11272–11277.
- (35) Clavel, M.; Goley, P. S.; Jain, N.; Zhu, Y.; Hudait, M. K. Strain Engineered Biaxial Tensile Epitaxial Germanium for High-Performance Ge/InGaAs Tunnel Field-Effect Transistors. *IEEE J. Electron Devices Soc.* **2015**, *3*, 184–193.
- (36) FIMMWAVE/FIMMPROP by Photon Design Ltd. <http://www.photond.com> (accessed March 2020).
- (37) Hudait, M. K.; Clavel, M.; Goley, P.; Jain, N.; Zhu, Y. Heterogeneous Integration of Epitaxial Ge on Si using AlAs/GaAs Buffer Architecture: Suitability for Low-power Fin Field-Effect Transistors. *Sci. Rep.* **2015**, *4*, 6964–6969.
- (38) Zhu, Y.; Maurya, D.; Priya, S.; Hudait, M. K. Tensile-Strained Nanoscale Ge/In<sub>0.16</sub>Ga<sub>0.84</sub>As Heterostructure for Tunnel Field-Effect Transistor. *ACS Appl. Mater. Interfaces* **2014**, *6*, 4947–4953.
- (39) Hudait, M. K.; Clavel, M. B.; Lester, L.; Saladukha, D.; Ochalski, T. J.; Murphy-Armando, F. Heterogeneously grown tunable group-IV laser on silicon. *Proc. SPIE* **2016**, 97550Y.
- (40) Saladukha, D.; Clavel, M. B.; Murphy-Armando, F.; Greene-Diniz, G.; Gruening, M.; Hudait, M. K.; Ochalski, T. J. Direct and indirect band gaps in Ge under biaxial tensile strain investigated by photoluminescence and photoreflectance studies. *Phys. Rev. B: Condens. Matter Mater. Phys.* **2018**, *97*, 195304-1–195304-12.
- (41) Hudait, M. K.; Clavel, M.; Goley, P.; Xie, Y.; Heremans, J. J. Magnetotransport Properties of Epitaxial Ge/AlAs Heterostructure Integrated on GaAs and Silicon. *ACS Appl. Mater. Interfaces* **2015**, *7*, 22315–22321.
- (42) Greene-Diniz, G.; Grüning, M. First-Principles Calculations of Band Offsets at Heterovalent  $\delta$ -Ge/In<sub>x</sub>Al<sub>1-x</sub>As Interfaces. *Phys. Rev. Appl.* **2018**, *10*, 044052.
- (43) Hudait, M. K.; Lin, Y.; Palmisiano, M. N.; Tivarus, C.; Pelz, J. P.; Ringel, S. A. Comparison of mixed anion, InAs<sub>1-y</sub>P<sub>y</sub> and mixed cation, In<sub>x</sub>Al<sub>1-x</sub>As metamorphic buffers grown by molecular beam epitaxy on (100) InP substrates. *J. Appl. Phys.* **2004**, *95*, 3952–3960.
- (44) Pavarelli, N.; Ochalski, T. J.; Murphy-Armando, F.; Huo, Y.; Schmidt, M.; Huyet, G.; Harris, J. S. Optical Emission of a Strained Direct-Band-Gap Ge Quantum Well Embedded Inside InGaAs Alloy Layers. *Phys. Rev. Lett.* **2013**, *110*, 17740.
- (45) People, P.; Bean, J. C. Calculation of critical layer thickness versus lattice mismatch for Ge<sub>x</sub>Si<sub>1-x</sub>/Si strained-layer heterostructures. *Appl. Phys. Lett.* **1985**, *47*, 322–324.
- (46) Ayers, J. E.; Kujofsa, T.; Rago, P.; Raphael, J. E. *Heteroepitaxy of Semiconductors: Theory, Growth, and Characterization*, 2nd ed.; CRC Press, Boca Raton, FL, 2017.
- (47) Dixon, R.; Goodhew, P. On the origin of misfit dislocations in InGaAs/GaAs strained layers. *J. Appl. Phys.* **1990**, *68*, 3163–3168.
- (48) Maree, P.; Barbour, J.; Van der Veen, J.; Kavanagh, K.; Bulle-Lieuwma, C.; Vieggers, M. Generation of misfit dislocations in semiconductors. *J. Appl. Phys.* **1987**, *62*, 4413–4420.
- (49) Kvam, E.; Hull, R. Surface orientation and stacking fault generation in strained epitaxial growth. *J. Appl. Phys.* **1993**, *73*, 7407–7411.
- (50) Petruzzello, J.; Leys, M. Effect of the sign of misfit strain on the dislocation structure at interfaces of heteroepitaxial GaAs<sub>x</sub>P<sub>1-x</sub> films. *Appl. Phys. Lett.* **1988**, *53*, 2414–2416.
- (51) Hirashita, N.; Sugiyama, N.; Toyoda, E.; Takagi, S.-I. Relaxation processes in strained Si layers on silicon-germanium-on-insulator substrates. *Appl. Phys. Lett.* **2005**, *86*, 221923.
- (52) Hwang, D.; Bhat, R.; Schwarz, S.; Chen, C. In *Partial Dislocations and Critical Thicknesses for Strained Layer Relaxation MRS Proceedings*; Cambridge Univ Press, 1992; p 421.
- (53) Hull, R.; Bean, J.; Peticolas, L.; Bahnck, D. Growth of Ge<sub>x</sub>Si<sub>1-x</sub> alloys on Si (110) surfaces. *Appl. Phys. Lett.* **1991**, *59*, 964–966.
- (54) Klingenstein, W.; Schweizer, H. Direct Gap Recombination in Germanium at High Excitation Level and Low Temperature. *Solid-State Electron.* **1978**, *21*, 1371–1374.
- (55) Guilloy, K.; Pauc, N.; Gassenq, A.; Niquet, Y. – M.; Escalante, J. – M.; Duchemin, I.; Tardif, S.; Dias, G. O.; Rouchon, D.; Widiez, J.; Hartmann, J. – M.; Geiger, R.; Zabel, T.; Sigg, H.; Faist, J.; Chelnokov, A.; Reboud, V.; Calvo, V. Germanium under High Tensile Stress: Nonlinear Dependence of Direct Band Gap vs Strain. *ACS Photonics* **2016**, *3*, 1907–1911.
- (56) Süess, M. J.; Geiger, R.; Minamisawa, R. A.; Schiefler, G.; Frigerio, J.; Chrastina, D.; Isella, G.; Spolenak, R.; Faist, J.; Sigg, H. Analysis of enhanced light emission from highly strained germanium microbridges. *Nat. Photonics* **2013**, *7*, 466–472.
- (57) Camacho-Aguilera, R. E.; Cai, Y.; Patel, N.; Bessette, J. T.; Romagnoli, M.; Kimerling, L. C.; Michel, J. An Electrically Pumped Germanium Laser. *Opt. Express* **2012**, *20*, 11316–11320.
- (58) Liu, J.; Sun, X.; Kimerling, L. C.; Michel, J. Direct-gap Optical Gain of Ge on Si at Room Temperature. *Opt. Lett.* **2009**, *34*, 1738–1740.
- (59) Jain, J. R.; Hryciw, A.; Baer, T. M.; Miller, D. A. B.; Brongersma, M. L.; Howe, R. T. A micromachining-based technology for enhancing germanium light emission via tensile strain. *Nat. Photonics* **2012**, *6*, 398–405.
- (60) Swaminathan, V.; Macrander, A. T. *Materials Aspects of GaAs and InP Based Structures*; Prentice Hall: Englewood Cliffs, NJ, 1991.
- (61) Schmidt, T.; Lischka, K. Excitation-power dependence of the near-band-edge photoluminescence of semiconductors. *Phys. Rev. B: Condens. Matter Mater. Phys.* **1992**, *45*, 8989–8994.
- (62) Arguirov, T.; Kittler, M.; Abrosimov, N. V. Room temperature luminescence from Germanium. *J. Phys.: Conference Series* **2011**, *281*, 012021–8.
- (63) Rideau, D.; Feraille, M.; Ciampolini, L.; Minondo, M.; Tavernier, C.; Jaouen, H.; Ghetti, A. Strained Si, Ge, and Si<sub>1-x</sub>Ge<sub>x</sub> alloys modeled with a first-principles-optimized full-zone k•p method. *Phys. Rev. B: Condens. Matter Mater. Phys.* **2006**, *74*, 195208.
- (64) Hybertsen, M. S.; Louie, S. G. Electron correlation in semiconductors and insulators: Band gaps and quasiparticle energies. *Phys. Rev. B: Condens. Matter Mater. Phys.* **1986**, *34*, 5390.
- (65) Zhang, S. B.; Yeh, C.-Y.; Zunger, A. Electronic structure of semiconductor quantum films. *Phys. Rev. B: Condens. Matter Mater. Phys.* **1993**, *48*, 11204.
- (66) Richard, S.; Aniel, F.; Fishman, G. Band diagrams of Si and Ge quantum wells via the 30-band k-p method. *Phys. Rev. B: Condens. Matter Mater. Phys.* **2005**, *72*, 245316-1–245316-7.